Comparison of measured and Monte Carlo calculated dose distributions from the NRC linac

Daryoush Sheikh-Bagheri[a)]
*Ionizing Radiation Standards, Institute for National Measurement Standards,
National Research Council Canada, Ottawa K1A 0R6, Canada
and Ottawa Carleton Institute of Physics, Carleton University, Ottawa, Ontario, Canada*

D. W. O. Rogers,[b)] Carl K. Ross, and Jan P. Seuntjens[c)]
*Ionizing Radiation Standards, Institute for National Measurement Standards,
National Research Council Canada, Ottawa K1A 0R6, Canada*

(Received 30 March 2000; accepted for publication 11 July 2000)

We have benchmarked photon beam simulations with the EGS4 user code BEAM [Rogers *et al.*, Med. Phys. **22**, 503–524 (1995)] by comparing calculated and measured relative ionization distributions in water from the 10 and 20 MV photon beams of the NRC linac. Unlike previous calculations, the incident electron energy is known independently to 1%, the entire extra-focal radiation is simulated, and electron contamination is accounted for. The full Monte Carlo simulation of the linac includes the electron exit window, target, flattening filter, monitor chambers, collimators, as well as the PMMA walls of the water phantom. Dose distributions are calculated using a modified version of the EGS4 user code DOSXYZ which additionally allows scoring of average energy and energy fluence in the phantom. Dose is converted to ionization by accounting for the $(\bar{L}/\rho)^{\text{water}}_{\text{air}}$ variation in the phantom, calculated in an identical geometry for the realistic beams using a new EGS4 user code, SPRXYZ. The variation of $(\bar{L}/\rho)^{\text{water}}_{\text{air}}$ with depth is a 1.25% correction at 10 MV and a 2% correction at 20 MV. At both energies, the calculated and the measured values of ionization on the central axis in the buildup region agree within 1% of maximum ionization relative to the ionization at 10 cm depth. The agreement is well within statistics elsewhere. The electron contamination contributes 0.35(±0.02) to 1.37(±0.03)% of the maximum dose in the buildup region at 10 MV and 0.26(±0.03) to 3.14(±0.07)% of the maximum dose at 20 MV. The penumbrae at 3 depths in each beam (in g/cm^2), 1.99 ($d_{\max}$, 10 MV only), 3.29 ($d_{\max}$, 20 MV only), 9.79 and 19.79, agree with ionization chamber measurements to better than 1 mm. Possible causes for the discrepancy between calculations and measurements are analyzed and discussed in detail.
[S0094-2405(00)00810-5]

Key words: Monte Carlo, BEAM, EGS4, experimental benchmark data, photon accelerator, 10 MV, 20 MV

I. INTRODUCTION

BEAM is a general purpose Monte Carlo code[1,2] for simulating radiotherapy beams from accelerators or ^{60}Co units. It is based on the EGS4 Monte Carlo code system.[3]

It is important to benchmark calculations with the BEAM code since it is being used by many researchers.[4–27] For example, the Lawrence Livermore National Laboratory's PEREGRINE[6,19,28] project uses the BEAM code to simulate the top end of the accelerator, and thus its results are based on BEAM.

In the original BEAM paper[1] there were extensive comparisons to electron beams and there are other papers with further careful electron comparisons.[5,29]

This work aims at benchmarking simulations of megavoltage photon beams using the BEAM Monte Carlo code. The independent knowledge of the electron beam energy, energy and intensity distributions, and divergence minimizes the number of unknown parameters in the comparison. More important, unlike commercial linacs used in other benchmarks, the NRC linac specifications are nonproprietary and are presented here to make it possible for other researchers to benchmark their simulations. Important questions are: how well can measured values of ionization be matched by Monte Carlo calculations, and, how do uncertainties in the beam model translate into uncertainties in the dose calculation in a water phantom and consequently in a patient?

The benchmark comparisons are done for 10 and 20 MV photon beams, using detailed comparisons with measurements of both central-axis depth-ionization and ionization profiles at three depths.

II. METHODS

A. The NRC linac and its model

The NRC linac is a Vickers research accelerator installed in 1968. It produces horizontal beams with energies between 4 and 40 MeV which are known to ±1%. By direct measurement with a magnetic spectrometer, the electron beam energy is known to have a Gaussian distribution with a full width at half maximum (FWHM) equal to 1% of the nominal energy.[30] The electron beam incident on the aluminum target is scanned on the surface of a cone with a measured half angle of 4.2°±0.3° to obtain field flatness. The apex of the

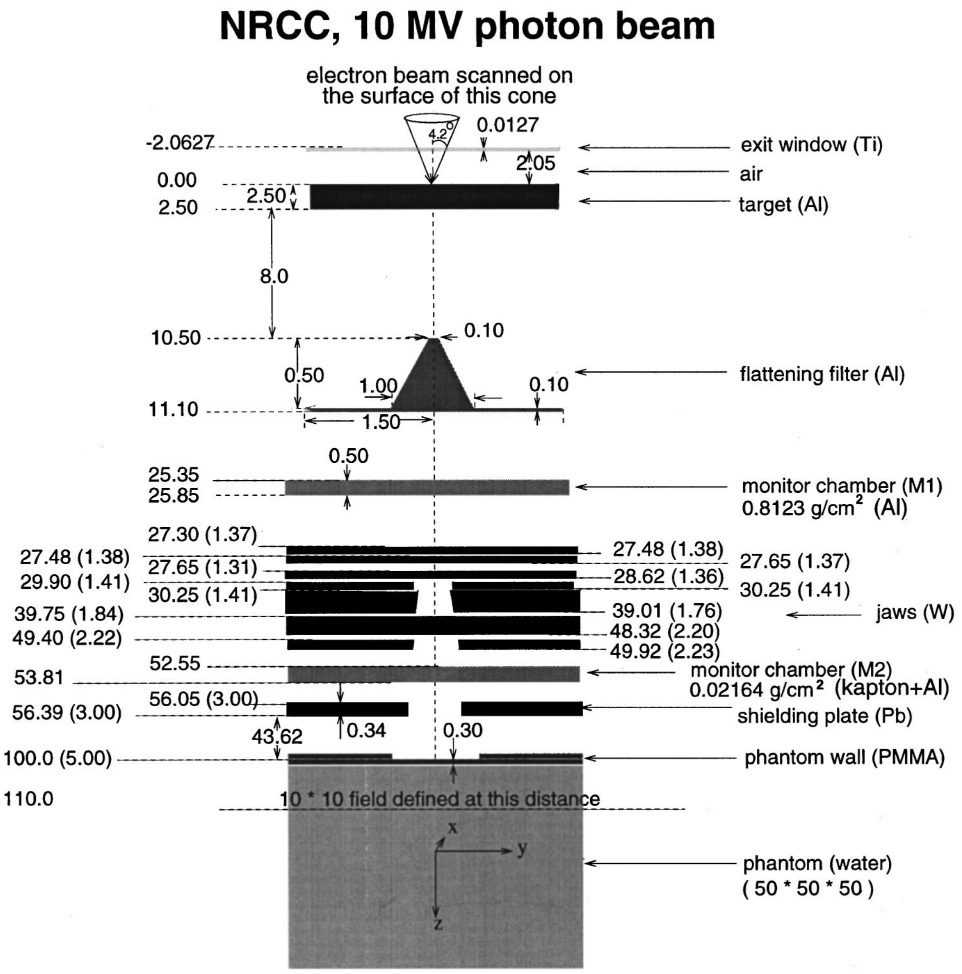

FIG. 1. Components of the accelerator as used to generate the 10 MV photon beam. All dimensions are in centimeters. Values in brackets are the distances from the central axis to the inner edges of the openings, for both *x*, and *y* collimators and have 0.05 cm uncertainty. The uncertainty in distances between the major components along the *z* axis is about 1 mm. The 20 MV beam is identical except that the aluminum target is 4.5 cm thick and there is no flattening filter.

cone is positioned on the front face of the target, but due to imperfections in the scanning coil, the apex wobbles. The wobble is estimated to occur inside a circle of 0.3 cm radius for the 10 MV beam and 0.2 cm for the 20 MV beams. The radial intensity profile of the electron beam is measured 11.5 cm upstream of the exit window using a profile monitor and found to be a Gaussian with an estimated FWHM of 0.35 cm for the 10 MV beam, and 0.25 cm for the 20 MV beam. The inherent divergence of the beam broadens this profile by about 0.05 cm so the width of the electron beam when it reaches the target is 0.4 and 0.3 cm for the 10 and 20 MV beams, respectively. To also include the effect of wobbling of the focal spot these Gaussians are convolved with circles of radii 0.3 and 0.2 cm, producing Gaussians with FWHM of 0.45 and 0.33 cm, respectively. The experimental uncertainty on these values is ±0.05 cm.

Two chambers are used to monitor the linac output (see Fig. 1). Monitor M1 is essentially made of aluminum with a total mass thickness of 0.8123 g/cm^2. Monitor M2, consists of six aluminum-coated layers of kapton with a total mass thickness of 0.021 64 g/cm^2.

The jaws (from a commercial Therac 20 accelerator) are nominally set to produce a geometrical $10\times 10\,\mathrm{cm}^2$ field at 10 cm depth inside the phantom (see Fig. 1). However, when the exact lateral position of each jaw is measured it is observed that the inner surfaces (the sides enclosing the beam) of the various sections of the jaws are not geometrically aligned on any side. A 0.34-cm-thick slab of lead with a $6\times 6\,\mathrm{cm}^2$ opening follows the monitor M2 to prevent backscatter into it. The front face of the water phantom (see Sec. II B 1) is placed at 100 cm SSD from the upstream surface of the target.

It is worth noting that the NRC beams are softer than many clinical beams of the same nominal energies because of the target material (aluminum rather than a high-Z material) and the flattening procedure (using beam sweeping rather than solely a flattening filter).

Figure 1 shows the model of the 10 MV beam setup which consists of the electron exit window, the aluminum target and flattening filter, the upstream monitor chamber, the tungsten jaws with their measured settings, the downstream monitor chamber, and the slab of lead. The jaws are assumed to be symmetrically set with respect to the central axis. The 20 MV beam setup is different in only two aspects: the target is thicker (4.5 cm) and no flattening filter is used.

To simulate the electron beam incident on the target properly, and to be able to investigate the effect of beam parameters (width, intensity distribution, divergence) a source routine (ISOURC15) has been written for BEAM. Figure 2 shows the swept beam source with radial distribution and diver-

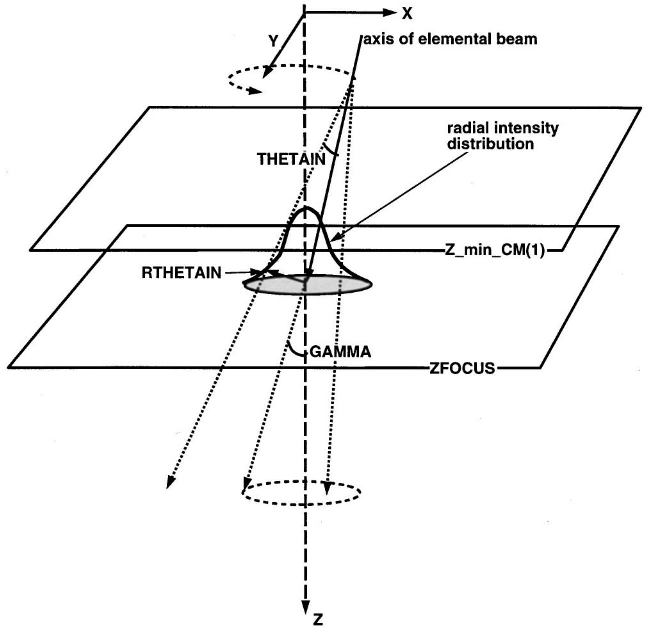

FIG. 2. The geometry of ISOURC=15 source, designed in this work. The beam sweeps on the surface of a cone with half-angle GAMMA and with the apex defined at ZFOCUS. The beam itself has a user-defined radial intensity distribution (in the case shown, a Gaussian), defined at ZFOCUS and in a plane perpendicular to the Z axis. The beam then diverges from this original distribution as if it originated at an imaginary point back along the axis of each elemental beam. The position of this imaginary point is defined by the divergence angle, THETAIN, and the radius (at ZFOCUS) at which the divergence angle is defined, RTHETAIN.

gence. The source routine allows one to sample incident electrons from a radially symmetric intensity distribution defined at a given plane perpendicular to the central axis (usually the apex of the sweeping cone). Additionally, it allows one to assign a radially increasing divergence to the beam and sweep the resulting beam on the surface of a cone with a given half angle. The divergence is specified as an angle at a certain radius (throughout this paper, the radius at half maximum) of the radial intensity distribution of the electron beam.

An accurate assessment of the beam divergence is not possible, but is estimated to be less than 5 mrad, which corresponds to a spread of 0.5 cm at 100 cm source-to-surface distance. An upper limit of 15 mrad can be set on the beam divergence based on the geometry of the beam pipe and focusing magnets.

The radial intensity distribution of the electron beam is modeled as a Gaussian with FWHM of 0.45 cm (for the 10 MV beam) and 0.33 cm (for the 20 MV beam). These values include the effects of the electron beam divergence and the wobbling of the focal spot.

The air between the jaws and the phantom, and the phantom itself are modeled using the code DOSXYZ (see Sec. II C 2).[1]

B. Ionization measurements

1. The water phantom

The phantom used for the ionization measurements is a $50\times50\times50\,\mathrm{cm}^3$ water tank with 1.72-cm-thick walls of PMMA, (density 1.19 g/cm^3). The beam enters the phantom horizontally and passes through a 0.3-cm-thick PMMA window, which bows by less than 0.02 cm due to water pressure. Since the reference depth is measured while the water is there, the distortion of the PMMA window is taken into account.

At each energy, four sets of ionization measurements are performed; a central-axis depth-ionization scan, and three horizontal scans at 1.99 ($d_{\max}$, 10 MV only), 3.29 ($d_{\max}$, 20 MV only), 9.79 and 19.79 g/cm^2. The depths are effective depths of measurement in accordance with the IAEA TRS-277 Code of Practice[31] and as discussed in Sec. II B 2. The scanner is computer controlled with a placement precision of about 0.05 cm. For comparisons, the measured horizontal profiles at each depth are shifted to be made symmetric with respect to the central axis using difference plots of measured and calculated (symmetrical) values.

2. The ion chamber and related corrections

The ion chamber used in this study is a Semiflex Tube Chamber (PTW, Freiburg, Germany, type 31002, formerly type 233642) serial number 396, with an active volume of 0.125 cm^3 and a cavity diameter of 0.55 cm. The ion chamber's energy response per unit absorbed dose, as specified by the manufacturer, shows about 4% over-response to energies below 150 keV compared to ^{60}Co. If the energy response is assumed to stay flat for energies above that of ^{60}Co, the over-response at lower energies results in a 1% over-response inside the field and 3% outside the field at 10 g/cm^2 depth for the 10 MV beam. This is because the calculated average energy of all photons at 10 g/cm^2 depth drops from around 1.3 MeV inside the field to below 300 keV, starting 1 cm outside the geometrical edge of the field. This is in good agreement with results measured by Fraass and van de Geijn.[32] The average energy calculation is done using the DOSXYZ code modified in this work (see Sec. II C 2).

The effective point of measurement for the ion chamber is taken to be $0.75r_{\mathrm{inner}}$ (where r_{inner} is the radius of the chamber cavity) upstream of the center of the chamber, consistent with the IAEA TRS-277 protocol.[31] The choice of offset is studied in the following.

The finite size of the detector has two effects: (a) perturbation effects, and (b) signal averaging effects.[33–40] The ion chamber not being water equivalent perturbs the electron fluence which would be present in the water in the absence of the ion chamber. For central-axis measurements this is taken into account by considering that the effective point of measurement of the chamber is further upstream and not at its center. When measuring profiles where there are highly nonlinear gradients, a correction is also necessary in principle. This issue is not addressed in the current protocols for radiotherapy and no correction is made here. Additionally, with a detector of finite size, such as an ion chamber, what is actually being measured is the signal averaged over its active volume. An upper limit on this effect is assessed by convolving (basically averaging) the calculated profile with a square step having a width equal to the diameter of the ion chamber. This upper limit on the spatial averaging effects of the ion chamber changes the assigned dose at the geometrical edges of the 10 MV profiles at depth of maximum ionization by up to 1.7% of maximum ionization and at 20 cm depth the correction is almost negligible. At 20 MV the correction is no larger than 0.8% of maximum ionization. These corrections are not included in the comparisons presented in the following but are estimated here to show that their maximum effects are not significant.

The ionization recombination correction, P_{ion}, for the chamber used in this study is assessed through the two voltage method[41] and is 1 to better than 0.5%. Due to its small effect, its variation with dose rate is ignored. The measured polarity correction factor is typically 0.1%. All the measurements are done with positive potential applied to the central electrode and variations in the polarity effect are ignored.

C. Monte Carlo simulations

1. Accelerator simulation with BEAM

a. Simulation parameters. Photons and electrons are transported down to energies of 0.01 and 0.7 MeV (including rest mass), respectively. When a particle's energy reaches these cutoff values, its energy is scored locally. Since low-energy electron transport constitutes a major part of the total CPU time for the simulation, BEAM's range rejection technique[1] is used. Anywhere outside the target, if the electron's total energy falls below 2.0 MeV (ESAVE) and its range does not allow it to escape the geometric region it is already traveling in, then it is discarded and its energy scored locally. The above value for ESAVE is selected since it provides a factor of 3 increase in speed and ignores only 0.1% of photons reaching the phantom surface, produced due to bremsstrahlung anywhere in the linac except in the target. Range rejection is turned off in the target, to provide the most accurate model for bremsstrahlung production.

Calculations were performed initially with both uniform bremsstrahlung splitting (UBS) and an improved variance reduction technique called selective bremsstrahlung splitting[2] (SBS). Dose distributions using both methods are the same within statistics. These calculations prove SBS is suitable for phase-space-based dose calculations. Subsequently, SBS is used in the rest of the simulations. Russian roulette of secondary electrons is not employed, since both photons as well as contaminant electrons are of interest in the dose calculations. When using UBS, a splitting factor of 30 is used, and the following parameters are used with SBS: $N_{\max}=200$, $N_{\min}=10$, and $R_f=11.3\,\text{cm}$. The use of SBS results in improvements in efficiency of up to a factor of 4 compared to UBS.[2]

b. Phase-space scoring. The linac simulation is run in parallel on 30 Pentium Pro 200 MHz processors. For the 10 MV beam, a total of 6×10^7 and for the 20 MV beam a total of 1×10^7 electron histories are simulated. The 10 MV simulation ran at 670 000 histories/h on each CPU, whereas at 20 MV, 160 000 histories/h per CPU could be simulated.

The linac simulation produces phase-space files scored at a plane right behind the lead shield located at $z=56.385\,\text{cm}$ (see Fig. 1).

For the 10 MV beam the phase-space files contain a total of 870 photon entries per 1000 electrons incident on the target. These entries have weights less than 1 and correspond to only 8 physical photons per 1000 incident electrons. At 20 MV the phase-space files contain 4000 photon entries which correspond to 27 actual photons per 1000 electrons incident on the target. The photon beam phase space files correspond to 1.3 and 1.7 Gbytes of data for the 20 and 10 MeV beams, respectively.

2. Calculations with DOSXYZ

DOSXYZ is a NRC EGS4 user code to calculate dose in Cartesian voxels.[1,42] The geometry used for the DOSXYZ calculations is shown in Fig. 3.

The phantom is divided into $3\times85\times41$ slices in the x, y, and z directions, respectively, resulting in 10 455 voxels ranging in volume from 0.03 to 104 cm^3. The unequal divisions are to minimize the total number of voxels while maintaining good resolution where needed. The phantom includes the air gap between the linac and the water tank as well as the PMMA wall of the tank. Central-axis depth-dose curves are calculated in the $2\times2\ \text{cm}^2$ region around the central axis. The width of the voxels in the penumbral region of the profiles is 0.1 cm.

In this work, DOSXYZ is modified to allow calculation of several physical quantities of interest in addition to dose, including the energy fluence and average energies of primary and phantom scattered photons.

Calculations using the DOSXYZ code are run in parallel on 30 CPUs producing 30 files for each quantity of interest. Each DOSXYZ calculation reads a corresponding phase-space file as input, recycling it less than 6 times for the 10 MV beam and less than 17 times for the 20 MV beam, and provides output files in ASCII format. These outputs are processed off-line to calculate the mean and standard deviations of each quantity using the array processing utility (SIGMA) of the PAW software (version 2.09/13) from CERN.[43] The statistical uncertainties in dose at the depth of maximum ionization and at a depth of 10 g/cm^2 are typically $\pm0.2\%$ (1 standard deviation).

Since an ion chamber measures ionization and not dose, the calculated values for dose have to be converted to ionization, by correcting them for a series of correction factors including the Spencer–Attix stopping-power ratio of water to air. No published photon beam dose distribution, that we are aware of, has taken account of the variation of stopping power with position. The value of dose in each voxel is divided by the corresponding value of $(\overline{L}/\rho)^{\text{water}}_{\text{air}}$ (see Sec. II C 3) to provide ionization. The variation of other correction factors with the position in the beam is ignored in this work and the value of the dose corrected for the ratio of stopping power of water to air is loosely called ionization.

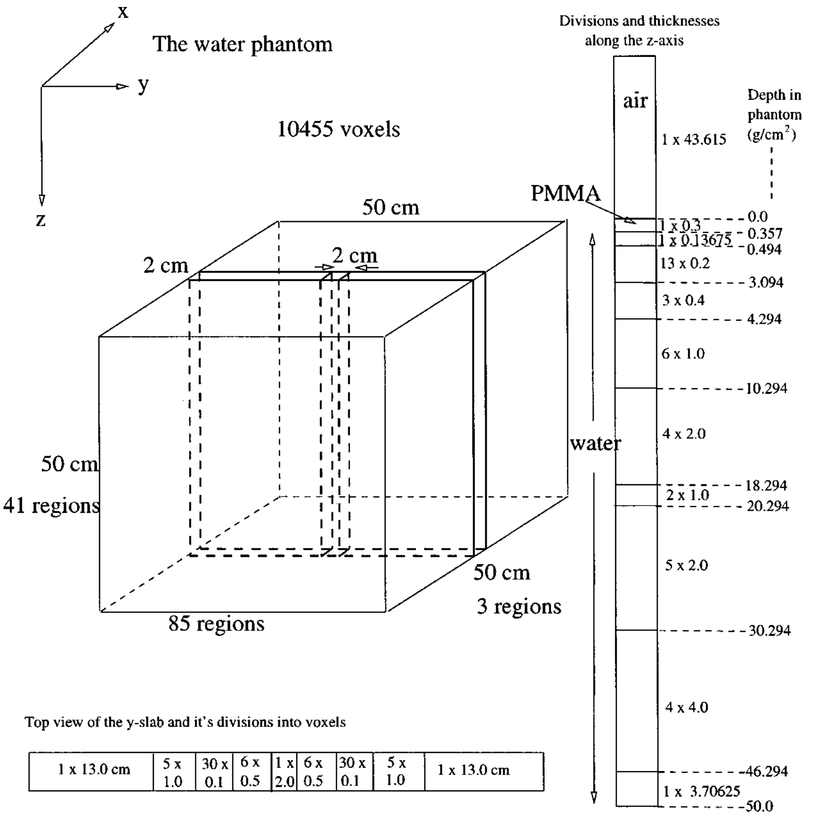

FIG. 3. Geometry used to calculate dose distributions with DOSXYZ and $(\overline{L}/\rho)^{\text{water}}_{\text{air}}$ distributions with SPRXYZ.

3. Stopping-power ratio calculations with SPRXYZ

A code called SPRXYZ was written, which is a hybrid of the NRC user-codes SPRRZ[44] and DOSXYZ. This code enables one to calculate Spencer–Attix stopping-power ratios for realistic photon and electron beams in a Cartesian geometry. Values of $(\overline{L}/\rho)^{\text{water}}_{\text{air}}$ calculated on the central axis using either SPRXYZ or SPRRZ show very good agreement, which gives confidence that the new code is working properly.

Calculations at 10 MV show that the variation of $(\overline{L}/\rho)^{\text{water}}_{\text{air}}$ with depth amounts to 1.25% over the entire depth of the phantom. The value of $(\overline{L}/\rho)^{\text{water}}_{\text{air}}$ starts at 1.119 ± 0.001 just past the PMMA wall, rapidly decreases to 1.114 ± 0.001 at depth of maximum ionization, has a value of 1.113 ± 0.001 at 10 cm depth, and then uniformly decreases to 1.106 ± 0.001 at 50 cm depth. The trend just discussed (an increase close to the surface and a very gradual decrease with increasing depth beyond depth of maximum ionization) is in agreement with calculations done by Andreo and Nahum.[45] Previous NRC calculations[46] of $(\overline{L}/\rho)^{\text{water}}_{\text{air}}$ which employed a point source emitting a 10 MV spectrum (from Mohan *et al.*[47]) from a 100 cm distant point in vacuum (i.e., having no electron contamination), were done using the NRC SPRRZ code, and calculated a value of 1.114 at the surface and a value of 1.107 at 15 cm depth. These values compared to the calculation performed in this work, show differences of up to 0.5% in the buildup region, mainly due to the electron contamination included in the present case. The difference between values of $(\overline{L}/\rho)^{\text{water}}_{\text{air}}$ inside and outside of the field in the 10 MV beam at the depth of maximum ionization, and at 10 and 20 cm depths, is 1.8%, 2%, and 2.7%, respectively.

At 20 MV the variation of $(\overline{L}/\rho)^{\text{water}}_{\text{air}}$ with depth amounts to 2% over the entire depth of the phantom. The value of $(\overline{L}/\rho)^{\text{water}}_{\text{air}}$ starts at 1.104 ± 0.001 just past the PMMA wall, rapidly decreases to 1.092 ± 0.001 at depth of maximum ionization, has a value of 1.091 ± 0.001 at 10 cm depth, and then uniformly decreases to 1.082 ± 0.001 at 50 cm depth. The value of $(\overline{L}/\rho)^{\text{water}}_{\text{air}}$ inside the field in the 20 MV beam at depth of maximum ionization, and at 10 and 20 cm depth, is 3.4%, 3.9%, and 4.5%, lower than outside the field, respectively.

Due to the very low energy of photons outside the field (see Sec. II B 2), the ion chamber is mainly detecting photons and not electrons, and therefore a correction for $(\overline{L}/\rho)^{\text{water}}_{\text{air}}$ in those regions may not be necessary. The $(\overline{L}/\rho)^{\text{water}}_{\text{air}}$ correction is applied throughout the phantom. Since the $(\overline{L}/\rho)^{\text{water}}_{\text{air}}$ is a relative correction, inside and outside the field, the absolute effect is so small that its effect on the dose cross profiles studied is not observable. For this reason the terms dose profile and ionization profile are used interchangeably.

4. Normalization and comparisons of data and uncertainties

The falloff region (starting at 1 cm past depth of maximum ionization) of both the calculated and the measured central-axis depth-ionization data are fit to a fourth-order polynomial using least squares. Typical values obtained for

χ^2 per degree of freedom are 0.6–0.7 at both energies. Using the fit, ionization data are normalized to a value of 1.0 at 10 g/cm^2 depth.

When comparing data sets which agree within a few percent but which vary considerably, it is essential to show a difference plot in order to see any systematic trends. Comparing Monte Carlo results is straightforward since the same bins are used and the uncertainties are just the sum of the statistical uncertainties (1 standard deviation) taken in quadrature. Comparisons of calculations and experiment are more complex. Measured data are taken to have a systematic uncertainty of 0.2% and are interpolated linearly to obtain values which correspond to the midpoints of Monte Carlo bins. The error bars shown are the sum of the statistical and systematic uncertainties (1 standard deviation) taken in quadrature. In the plots, any points without error bars are points for which no measured data are available.

D. Factors studied

1. Electron beam energy

One advantage of using the NRC linac in the benchmark study is that the electron beam energy is known to better than 1%, so it is not taken as a parameter. However, when the nominal beam energy is varied by 3% at 10 MV and 5% at 20 MV, it is observed that, unlike the peripheral dose (dose outside the penumbra), the dose distribution inside the field and in the penumbral region are sensitive to such variations. The beam energy, as one expects, also impacts the depth-ionization distribution and the calculations show that, for example, increasing the electron energy from 20 to 21 MeV changes the value of relative ionization at 10 g/cm^2 depth, from 0.788±0.001 to 0.796±0.001.

2. Electron beam energy distribution

To assess if the electron beam energy distribution (which is taken as a Gaussian) has an observable effect on the dose distribution, a calculation done with a monoenergetic 20 MV beam is compared to our Gaussian model (with 1% energy spread) and no statistically significant differences in the central axis depth dose or dose profiles are observed at the 1% (1σ) statistics level.

3. Electron beam radial intensity distribution

Figure 4 shows the effect, for the 10 MV photon beam, of ignoring the radial intensity distribution of the electron beam and simulating it as a pencil beam of radius 0.001 cm, instead of as a Gaussian with FWHM of 0.45 cm, which has an uncertainty of only ±0.05 cm. This comparison demonstrates the necessity of modeling the electron beam radial intensity distribution and that the measured values are clearly known well enough. As expected, the penumbral width gets wider when the source size is increased, making the profiles systematically different in the penumbral region.

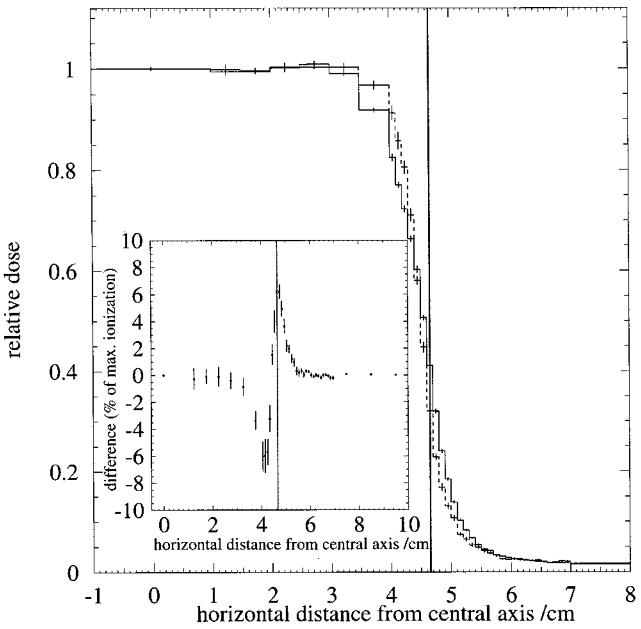

FIG. 4. Comparison of the dose profiles calculated at depth of maximum ionization in the 10 MV photon beam with (solid line) and without (dashed line) modeling the intensity distribution of the incident electron beam on the exit window. There are statistically significant differences, as shown by the inset, both inside and outside the geometrical edges of the field (vertical lines). Error bars here and elsewhere correspond to 1 standard deviation estimates of the overall uncertainty (see Sec. II C 4).

4. Electron beam sweeping angle and divergence

Calculations for the 20 MV beam with the sweeping turned off (i.e., zero sweeping angle) show that the sweeping angle has an immense effect on the entire shape of the profile. To check the sensitivity of the calculations to the sweeping angle more closely, the sweeping angle is changed from 4.2° to 4.1°. Calculated dose profiles at $d_{\max}$ in the 20 MV beam with the sweeping angle of 4.1° are higher by up to 3% in the shoulder region, i.e., inside the geometrical edges of the field, but not different outside. This provides a more precise estimate for the sweeping angle and shows that it must be 4.2±0.05° (compare to the estimate of 4.2±0.3° from measurement, see Sec. II A).

As discussed before, a reasonable estimate for the electron beam divergence for the NRC linac is about 5 mrad. A calculation at 20 MV, with a 15 mrad divergent electron beam (worst possible case), only shows differences inside the field and these are less than 0.8% of maximum ionization. However, using the 5 mrad estimate, there is no observable effect from including the beam divergence in the model.

5. Electron multiple scattering in the target

To see whether the results are sensitive to the details of the electron multiple scattering in the target, ESTEPE (the fractional energy loss per step)[48] was reduced to 0.5%. Reduction of ESTEPE results in smaller electron multiple-scattering step sizes. The step size, which by default is determined by the PRESTA algorithm,[49] depends on the dimensions of the voxels. Selection of the step size by

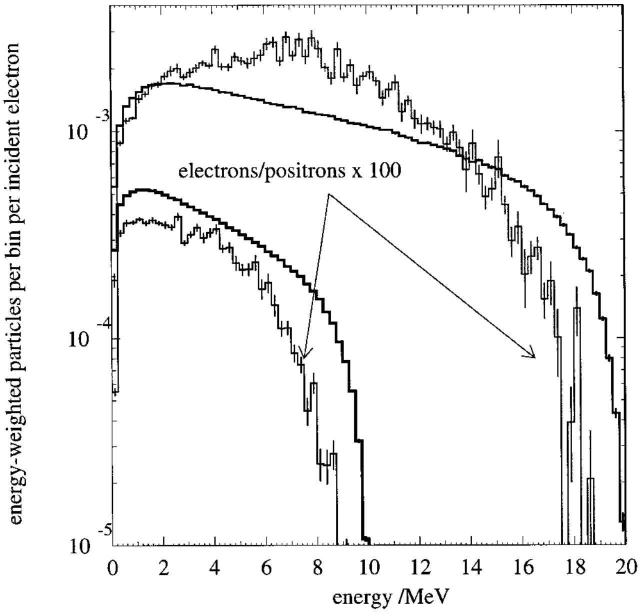

FIG. 5. Energy-weighted number of photons (thick histograms) and electrons (thin histograms) differential in energy for both the 10 and 20 MV photon beams calculated for all particles reaching a scoring plane at 100 cm SSD. The histograms are normalized per incident electron on the target. All the bins are 250 keV wide.

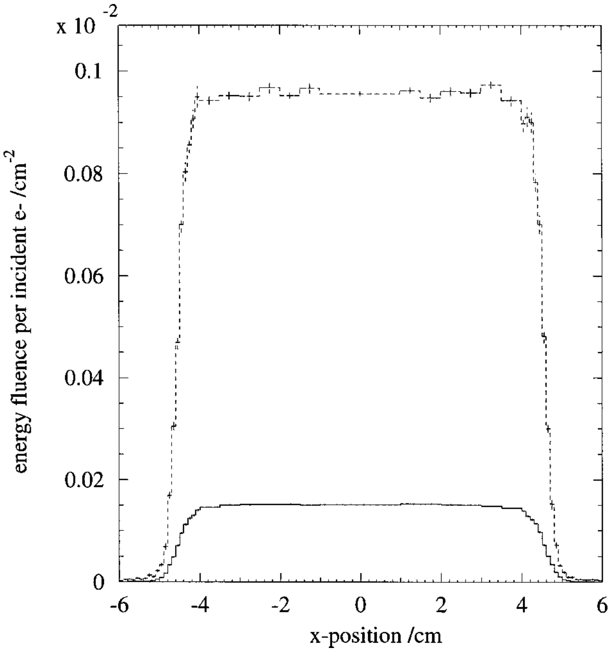

FIG. 6. Photon energy fluence distributions at 100 cm SSD for the 10 (solid line) and 20 MV (dashed line) beams, for a 2-cm-wide strip centered on the *y* axis.

PRESTA can lead to energy losses per step of typically a few percent (7% at 10 MeV in tungsten), or even 25% in large regions in water. The results show no sensitivity to ESTEPE at the 1% (1σ) statistics level.

6. Secondary collimators

Since the inner surfaces of the secondary collimators are not necessarily aligned, the opening of each individual jaw at both the upstream and downstream faces are measured and the measurements used in the simulations. The uncertainty on these measurements is 0.05 cm. Shifts of 0.05 cm in the lateral position of the back of the upstream jaw, located at $z=39.01$ cm, changes the ionization in the penumbral region by up to 8% of maximum ionization (and could reverse the sign of the 4% discrepancy seen in Fig. 11).

Since the penumbra is partially shaped by transmission through the edges of the jaws the exact composition of the jaw might have observable effects. The composition of the jaws is varied from pure tungsten to a tungsten alloy (10.7% Cu, 32.2% Ni, 57.1% W, by weight) and no difference is observed in the profiles.

The primary transmission through the bulk of each of the jaws is estimated to be negligible (less than 0.03% through 10 cm of W).

III. RESULTS

A. Phase-space analysis

The phase-space data scored at the phantom surface (in addition to those scored behind the jaws), provide histograms of absolute numbers of energy weighted photons and electrons differential in energy (Fig. 5) photons and differential in position (Fig. 6).

Note that the phase-space files analyzed in Figs. 5 and 6 are 9 times smaller than those used in the dose calculations. At both energies the statistical uncertainty in the photon fluence inside the field, for the phase-space files used in the dose calculations, is about 0.2% (for a 1 cm^2 region).

B. Central-axis depth ionization

1. The 10 MV photon beam

Figures 7 and 8 show comparisons of the Monte Carlo calculated values of central-axis depth-ionization curves with the ion chamber measured values corrected for the effective point of measurement, for the 10 MV beam. The agreement past depth of maximum ionization is better than 0.7% of local ionization (with a statistical precision of 0.2%–0.5%). On account of the normalization procedure used here, the effect of the correction factors shows up mostly in the buildup region (see Figs. 8 and 9). Correcting for the effective point of measurement has much greater impact on the depth-ionization curve than correcting for $(\overline{L}/\rho)_{\rm air}^{\rm water}$. For example, if we vary the effective point of measurement we find that using a shift of $0.6r_{\rm inner}$ upstream of the center of the ion chamber gives the best agreement and the agreement in the buildup region becomes better than 0.45% of local ionization (see Fig. 9). The value of $0.6r_{\rm inner}$ is in agreement with the new recommendations of the IAEA[50] and AAPM[51] however, it is only used in this paper when explicitly specified.

At 10 MV, the calculated value for the ratio of dose on central axis at 10 g/cm^2 depth to that at depth of maximum ionization is 0.682 ± 0.001 and that of ionization is 0.683 ± 0.001. The measured value is 0.682 ± 0.002 (0.689 ± 0.002 if the effective point of measurement is ignored).

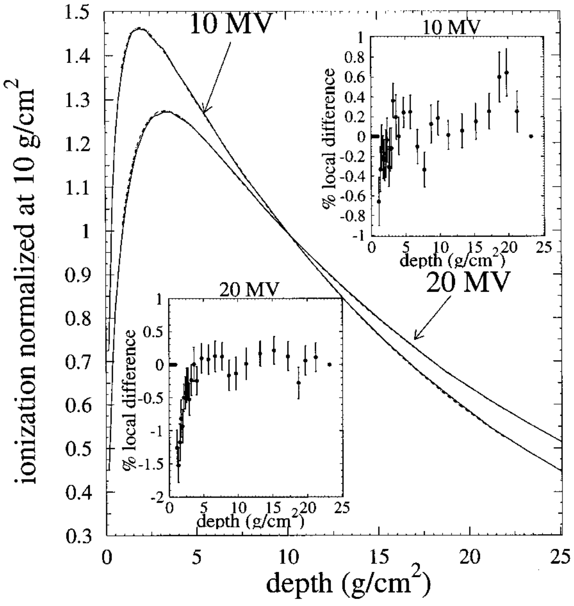

FIG. 7. Comparison of the calculated (solid lines) and measured (dashed lines) depth-ionization curves in the 10 and 20 MV photon beams. All curves are normalized to a depth of 10 g/cm^2 using a fourth-order polynomial fit. The measurements are corrected for the effective point of measurement using a shift equal to $0.75\times r_{\mathrm{inner}}$, upstream of the center of the ion chamber.

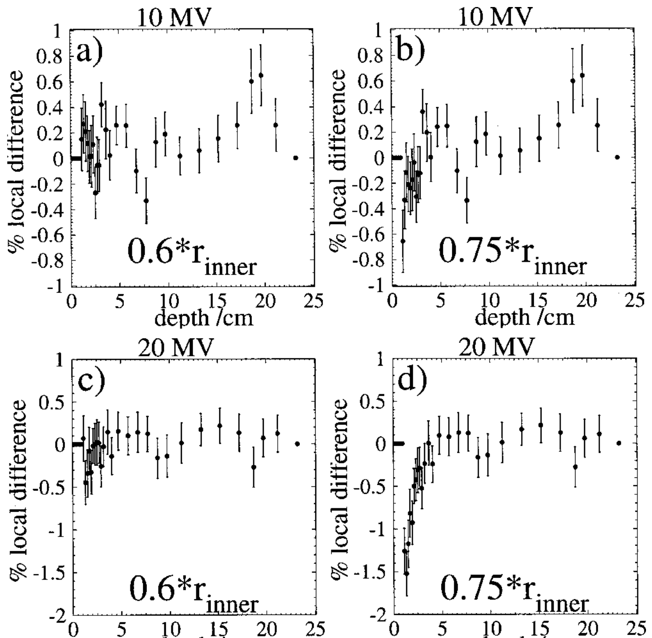

FIG. 9. Percentage differences in the calculated and measured central-axis depth ionization curves for the 10 and 20 MV beams, when the shift upstream of the center of the ion chamber related to the effective point of measurement is taken as $0.6r_{\mathrm{inner}}$ [(a) and (c)], and when it is taken as $0.75r_{\mathrm{inner}}$ [(b) and (d)]. The 20 MV beam clearly demonstrates that the former choice results in much better agreement in the buildup region.

The uncertainty estimates on the measured values are based on an estimate of 0.05 cm uncertainty in the position. In the 10 MV beam, the ratio of the dose at 20 g/cm^2 to that at 10 g/cm^2, D_{20}/D_{10}, is 0.587 ± 0.001 based on the calculations and 0.584 ± 0.002, based on the measurements. The dose from contaminant electrons constitutes $1.37\pm0.03\%$ of maximum dose on the surface of the phantom (in the PMMA window) and $0.35\pm0.02\%$ of maximum dose at the depth of maximum ionization.

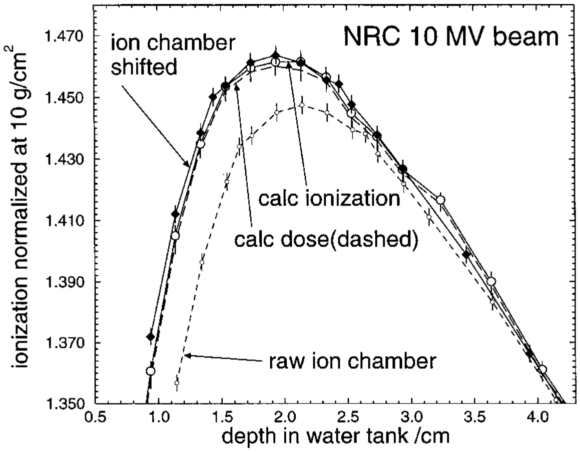

FIG. 8. Comparison of the calculated (solid line, open circles) and measured (solid line, filled circles) depth-ionization curves in water for the 10 MV beam in the buildup region. These measured values are corrected for the effective point of measurement using a shift equal to $0.75r_{\mathrm{inner}}$, upstream of the center of the ion chamber. All curves are normalized at a depth of 10 g/cm^2 using a fourth-order polynomial fit. The calculated depth-dose curve (long dash line) and the measured ionization not corrected for the effective point of measurement (short dash line) are also shown. The calculated curve for ionization is obtained by dividing the calculated values of dose by values of $(\bar{L}/\rho)^{\mathrm{water}}_{\mathrm{air}}$ calculated using the SPRXYZ code.

2. The 20 MV photon beam

At 20 MV the depth-ionization curves agree to better than 0.3% of local ionization past depth of maximum ionization, and to better than 1.55% of local ionization in the buildup region (see Figs. 7 and 10).

Although correcting for the $(\bar{L}/\rho)^{\mathrm{water}}_{\mathrm{air}}$ has a minor effect compared to the effect of the effective point of measurement, nonetheless, it has an observable effect and it slightly wors-

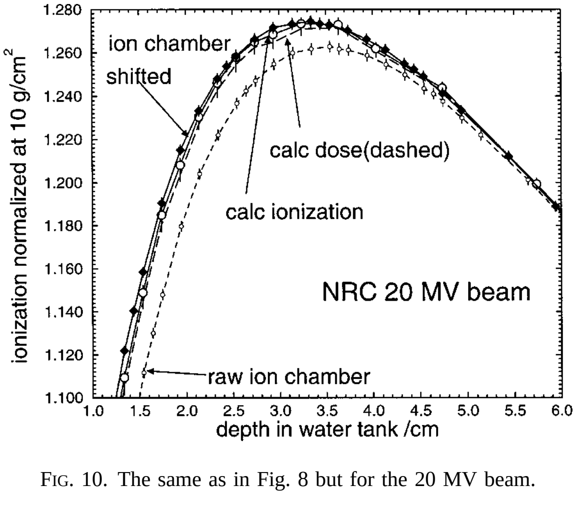

FIG. 10. The same as in Fig. 8 but for the 20 MV beam.

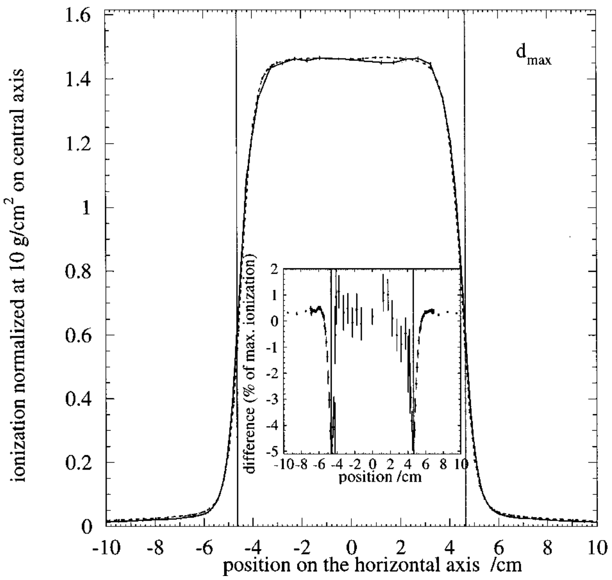

FIG. 11. Comparison of the calculated (solid line) and measured (dashed line) ionization profiles at depth of maximum ionization (1.99 g/cm^2) for the 10 MV photon beam. Both curves are normalized to the value of ionization at 10 g/cm^2 depth on central axis. The vertical lines show the geometrical edges of the field in the model.

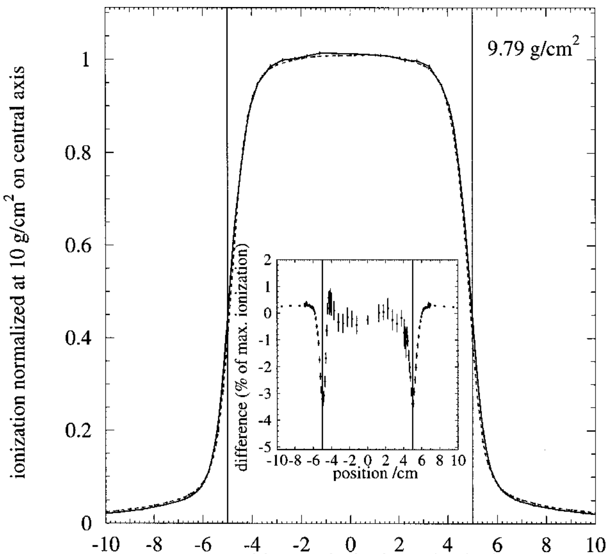

FIG. 12. The same as in Fig. 11 but at 9.79 g/cm^2 depth for the 10 MV photon beam.

ens the agreement in the buildup region if the shift for the effective point of measurement is taken as $0.75r_{\text{inner}}$. As in the case of the 10 MV photon beam, correcting for the effective point of measurement has much greater impact on the depth-ionization curve than correcting for $(\overline{L}/\rho)^{\text{water}}_{\text{air}}$. If we vary the effective point of measurement we find that using a shift of $0.6r_{\text{inner}}$ upstream of the center of the ion chamber gives the best agreement and the agreement in the buildup region becomes better than 0.5% of local ionization (see Fig. 9).

At 20 MV, the calculated value for the ratio of the dose on central axis at 10 cm depth to that at depth of maximum ionization is 0.787 ± 0.001 and that of ionization is 0.788 ± 0.001. The measured value is 0.785 ± 0.002 (ignoring the effective point of measurement this value would be 0.792 ± 0.002). In the 20 MV beam, the ratio of dose at 20 g/cm^2 to that at 10 g/cm^2, D_{20}/D_{10}, is 0.641 ± 0.001, based on the calculations, and 0.642 ± 0.002, based on the measurements. The dose from contaminant electrons constitutes $3.14 \pm 0.07\%$ of maximum dose on the surface of the phantom (in the PMMA window) and $1.20 \pm 0.03\%$ of maximum dose at depth of maximum ionization.

It is interesting to note that none of the factors studied in Sec. II D affects the calculated value of %dd(10), except, of course, the electron beam energy.

C. Ionization profiles

1. The 10 MV photon beam

Figures 11, 12, and 13 show comparisons between measured and calculated ionization profiles at 1.99($d_{\max}$), 9.79, and 19.79 g/cm^2 respectively. The agreement between calculations and measurements is better than 1% (of maximum ionization), out to 1 cm inside the geometrical edges of the field. As one approaches the penumbra, the agreement worsens at all depths. The worst case is at the depth of maximum ionization (see Fig. 11), where maximum differences of about 5% (of maximum ionization) are present. Because of the very steep dose fall-off in the penumbra, a slight misalignment of the jaws can lead to differences of the order seen here (see Sec. II D 6). The discrepancy between the position of the calculated and the measured penumbrae is about 0.05 cm at the depth of maximum ionization, and a maximum of 0.15 cm at 19.79 g/cm^2 depth. The discrepancy in the peripheral dose distributions is about 0.3% (of maximum ionization) at depth of maximum ionization, but it reduces to less than 0.2% (of maximum ionization) at 19.79 g/cm^2 depth.

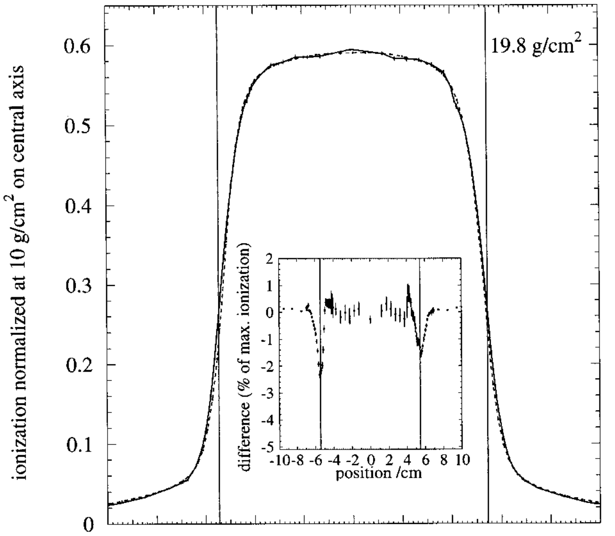

FIG. 13. The same as in Fig. 11 but at 19.8 g/cm^2 depth for the 10 MV photon beam.

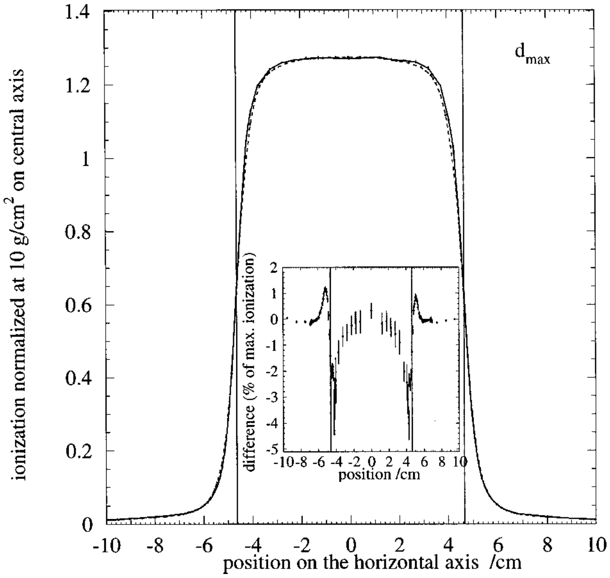

FIG. 14. The same as in Fig. 11 but at $d_{\max}=3.3$ g/cm^2 depth for the 20 MV photon beam.

2. The 20 MV photon beam

The calculated profiles at 20 MV show essentially the same kind of agreement with the measurements as at 10 MV. Figure 14 shows the comparison at depth of maximum ionization.

The discrepancy around the geometrical edges is evident in this case too, but the profiles match slightly better in the regions well outside the edge.

IV. DISCUSSION AND CONCLUSIONS

A very precise set of benchmark comparisons of Monte Carlo calculated dose distributions in 10 and 20 MV photon beams have been performed. The agreement between calculations and measurements on the central axis for both beam energies is generally better than 0.5% of maximum ionization. The correction for the effective point of measurement has a greater impact on the central-axis depth ionization than the variation of $(\overline{L}/\rho)^{\text{water}}_{\text{air}}$. In accordance with the IAEA protocol[31] the measured values for depth ionization were initially shifted upstream by 0.75 times the cavity radius of the chamber. This leads to discrepancies of up to 1.5% between the measurements and the calculations in the buildup region. However, if the factor multiplying the cavity radius is changed from 0.75 to 0.6, the agreement in the buildup region becomes better than 0.5% of maximum ionization, even for the 20 MV beam. These data provide strong support for the change to a shift of $0.6r_{\text{inner}}$.

The stopping power ratio is calculated using the realistic photon beam in a geometry identical to that used in the dose calculations. In the simulations, best estimates for the physical parameters involved are used and the sensitivity of the dose distribution to the uncertainties in these parameters was studied. Effort has been put into understanding the factors influencing the penumbral shape. The lack of knowledge about the *exact jaw setting* is a dominant factor which causes discrepancies between the simulation and the measurement in the penumbral region. Although the distance between each pair of jaws is measured at two points (one upstream and one downstream) to an accuracy of better than 0.05 cm, this accuracy is not good enough. As an example, if the edge of the jaw located at 39.01 cm is deliberately shifted by 0.05 cm toward the central axis (i.e., the opening is moved from 1.76 to 1.71 cm), then the direction of the discrepancy at the geometrical edges reverses in Figs. 11–13. Although this uncertainty leads to relatively large discrepancies in terms of absolute dose, as a positional shift it is of the order of 1 mm or less.

The electron beam intensity distribution and sweeping angle are two other important factors influencing the penumbral shape in the beams. The FWHM of the electron beam intensity distributions is estimated with an accuracy of 0.05 cm and although ignoring the intensity distribution altogether affects the penumbra, uncertainties of this size cause little uncertainty in calculated profiles.

Reduction of ESTEPE to 0.5%, from the default value defined by the PRESTA algorithm, shows no difference in the dose distributions, indicating that the results are not sensitive to the details of electron multiple scattering in the target.

Inside the field out to 1 cm from the geometrical edges of the field, the calculated ionization profiles agree with measurements to better than 1.2% of maximum ionization. The agreement outside the field is better than 0.5% of maximum ionization. The agreement around the geometrical edges is better than 5% of maximum ionization and any agreement better than this, in that region, is likely coincidental and due to counteracting effects of a series of inaccuracies in the simulation parameters used in the linac model.

The general conclusion is that the BEAM code is capable of very accurately simulating photon beams generated by electron accelerators but that accurate information about both the accelerator head and the incident electron beam are needed.

ACKNOWLEDGMENTS

We would like to thank CERN for providing us with the PAW software, Dr. Michel Proulx of NRC for his expertise in computer network management, and Blake Walters for support of the BEAM system. This work was partially supported by NCI Grant No. R01 CA52692.

[a] Present address: MDS Nordion, Kanata, Ontario, Canada.

[b] Electronic mail: dave@irs.phy.nrc.ca

[c] Present address: McGill University, Montreal General Hospital, Montreal, Quebec, Canada.

[1] D. W. O. Rogers, B. A. Faddegon, G. X. Ding, C. M. Ma, J. Wei, and T. R. Mackie, ''BEAM: A Monte Carlo code to simulate radiotherapy treatment units,'' Med. Phys. **22**, 503–524 (1995).

[2] D. W. O. Rogers, C. M. Ma, G. X. Ding, B. Walters, D. Sheikh-Bagheri, and G. G. Zhang, BEAM98 Users Manual, NRC Report PIRS 509(a)revC (1998).

[3] W. R. Nelson, H. Hirayama, and D. W. O. Rogers, The EGS4 Code System, Report SLAC-265, Stanford Linear Accelerator Center, Stanford, California, 1985.

[4] G. X. Ding and D. W. O. Rogers, Energy spectra, angular spread, and dose distributions of electron beams from various accelerators used in

radiotherapy, National Research Council of Canada Report PIRS-0439 (see http://www.irs.inms.nrc.ca/inms/irs/papers/PIRS439/pirs439.html) (1995).

[5] G. X. Ding, D. W. O. Rogers, and T. R. Mackie, ''Mean energy, energy-range relationship and depth-scaling factors for clinical electron beams,'' Med. Phys. **23**, 361–376 (1996).

[6] C. L. Hartmann-Siantar, P. M. Bergstrom, W. P. Chandler, L. Chase, L. J. Cox, T. P. Daly, D. Garrett, S. M. Hornstein, R. K. House, E. I. Moses, R. W. Patterson, J. A. Rathkopf, and A. Schach von Wittenau, Lawrence Livermore National Laboratory's PEREGRINE project, in *Proceedings of the XII-th Conference on the Use of Computers in Radiotherapy*, May 27–30, 1997 (Medical Physics Publishing, Madison, 1997), pp. 19–22.

[7] H. Neuenschwander, W. Volken, C. Cris, R. Mini, and P. Schwab, ''Fast Monte Carlo algorithms for electron beam treatment planning,'' in *Proceedings of the XII-th Conference on the Use of Computers in Radiotherapy*, May 27–30, 1997 (Medical Physics Publishing, Madison, 1997), p. 23–26.

[8] C. M. Ma, B. A. Faddegon, D. W. O. Rogers, and T. R. Mackie, ''Accurate characterization of Monte Carlo calculated electron beams for radiotherapy,'' Med. Phys. **24**, 401–416 (1997).

[9] J. Siebers, B. Libby, and R. Mohan, ''Trust, but verify: comparison of MCNP and BEAM Monte Carlo codes for generation of phase space distributions for a Varian 2100C,'' Med. Phys. **25**, A143 (1998).

[10] F. Verhaegen, I. J. Das, and H. Palmans, ''Monte Carlo dosimetry study of a 6 MV stereotactic radiosurgery unit,'' Phys. Med. Biol. **43**, 2755–2768 (1998).

[11] K. M. Ayyangar and S. B. Jiang, ''Do we need Monte Carlo treatment planning for linac based radiosurgery? A case study,'' Med. Dosim. **23**, 161–168 (1998).

[12] M. Glass, T. Mackie, and G. Fang, ''Monte Carlo models for tomotherapy,'' Med. Phys. **25**, A143 (1998).

[13] B. A. Faddegon, J. Balogh, R. Mackenzie, and D. Scora, ''Clinical considerations of Monte Carlo for electron radiotherapy treatment planning,'' Rad. Phys. Chem. **53**, 217–227 (1998).

[14] A. Kapur, C.-M. Ma, E. C. Mok, and A. L. Boyer, ''Monte Carlo calculations of electron beam output factors for a medical linear accelerator,'' Phys. Med. Biol. **43**, 3479–3494 (1998).

[15] M. Bieda, J. Antolak, and K. Hogstrom, ''Monte Carlo method for commissioning electron beams,'' Med. Phys. **25**, 1577 (1998).

[16] G. Mora, A. Maio, and D. W. O. Rogers, ''Monte Carlo simulation of a typical ^{60}Co therapy source,'' Med. Phys. **26**, 2494–2502 (1999).

[17] F. Verhaegen, A. E. Nahum, S. V. de Putte, and Y. Namito, ''Monte Carlo modelling of radiotherapy kV x-ray units,'' Phys. Med. Biol. **44**, 1767–1789 (1999).

[18] H. Palmans, W. Mondelaers, and H. Thierens, ''Absorbed dose beam quality correction factors k_Q for the NE2571 chamber in a 5 MV and 10 MV photon beam,'' Phys. Med. Biol. **44**, 647–663 (1999).

[19] A. Schach von Wittenau, L. J. Cox, P. M. Bergstrom, W. P. Chandler, C. L. Hartmann-Siantar, and R. Mohan, ''Correlated histogram representation of Monte Carlo derived medical accelerator photon-output phase space,'' Med. Phys. **26**, 1196–1211 (1999).

[20] J. V. Siebers, P. J. Keall, B. Libby, and R. Mohan, ''Comparison of EGS4 and MCNP4b Monte Carlo codes for generation of photon phase space distributions for a Varian 2100C,'' Phys. Med. Biol. **44**, 3009–3026 (1999).

[21] C.-M. Ma, E. Mok, A. Kapur, T. Pawlicki, D. Findley, S. Brain, and K. Forster, ''Clinical implementation of a Monte Carlo treatment planning system,'' Med. Phys. **26**, 2133–2143 (1999).

[22] M. G. Karlsson, M. Karlsson, and C.-M. Ma, ''Treatment head design for multileaf collimated high-energy electrons,'' Med. Phys. **26**, 2161–2167 (1999).

[23] R. Sjögren, M. G. Karlsson, and M. Karlsson, ''Methods for the determination of effective monitor chamber thickness,'' Med. Phys. **26**, 1871–1873 (1999).

[24] R. A. C. Siochi, ''Requirements for Manufacturer Supplied Data for Monte Carlo Simulation: A BEAM Perspective,'' *Proceedings of the Fifteenth International Conference on the Applications of Accelerators in Research and Industry* (The American Institute of Physics, Melville, 1999) pp. 1060–1065.

[25] K. D. Vlamynck, H. Palmans, F. Verhaegen, C. D. Wagter, W. D. Neve, and H. Thierens, ''Dose measurements compared with Monte Carlo simulations of narrow 6 MV multileaf collimator shaped photon beams,'' Med. Phys. **26**, 1874–1882 (1999).

[26] P. J. Keall, J. V. Siebers, R. Jeraj, and R. Mohan, ''The effect of dose calculation uncertainty on the evaluation of radiotherapy plans,'' Med. Phys. **27**, 478–484 (2000).

[27] B. A. Faddegon and I. Blevis, ''Electron spectra derived from depth dose distributions,'' Med. Phys. **27**, 514–526 (2000).

[28] A. Schach von Wittenau, P. M. Bergstrom, and L. J. Cox, ''Patient-dependent beam-modifier physics in Monte Carlo photon dose calculations,'' Med. Phys. **27**, 935–947 (2000).

[29] G. X. Ding and D. W. O. Rogers, Monte Carlo simulation of NPL linac and calculation of dose distributions and water/air stopping-power ratios, National Research Council of Canada Report PIRS 0399 (1993).

[30] M. S. MacPherson and C. K. Ross, A Magnetic Spectrometer for Electron Energy Calibration, NRC Report PIRS 617 (1998).

[31] IAEA, *Absorbed Dose Determination in Photon and Electron Beams; An International Code of Practice*, Vol. 277 of *Technical Report Series* (IAEA, Vienna, 1987).

[32] B. A. Fraass and J. van de Geijn, ''Peripheral dose from megavolt beams,'' Med. Phys. **10**, 809–818 (1983).

[33] C. H. Sibata, H. C. Mota, A. S. Beddar, P. D. Higgins, and K. H. Shin, ''Influence of detector size in photon beam profile measurements,'' Phys. Med. Biol. **36**, 621–631 (1991).

[34] F. Garcia-Vicente, J. M. Delgado, and C. Peraza, ''Experimental determination of the convolution kernel for the study of the spatial response of a detector,'' Med. Phys. **25**, 202–207 (1998).

[35] P. Charland, E. El-Khatib, and J. Wolters, ''The use of deconvolution and total least squares in recovering a radiation detector line spread function,'' Med. Phys. **25**, 152–160 (1998).

[36] P. D. Higgins, C. H. Sibata, L. Siskind, and J. W. Sohn, ''Deconvolution of detector size effect for small field measurement,'' Med. Phys. **22**, 1663–1666 (1995).

[37] D. Jones, ''Comparison of the perturbation correction in a parallel plate and a cylindrical ion chamber,'' Med. Phys. **8**, 239–241 (1981).

[38] K.-S. Chang, F.-F. Yin, and K.-W. Nie, ''The effect of detector size to the broadening of the penumbra–a computer simulated study,'' Med. Phys. **23**, 1407–1411 (1996).

[39] R. K. Rice, J. H. Hansen, G. K. Svensson, and R. L. Siddon, ''Measurements of dose distributions in small beams of 6 MV x-rays,'' Phys. Med. Biol. **32**, 1087–1099 (1987).

[40] F.-F. Yin, ''Physical penumbra change of beam profile due to film digitization,'' Med. Phys. **22**, 803–805 (1995).

[41] AAPM TG-21, ''A protocol for the determination of absorbed dose from high-energy photon and electron beams,'' Med. Phys. **10**, 741–771 (1983).

[42] C. M. Ma, D. W. O. Rogers, and B. Walters, DOSXYZ99 Users Manual, NRC Report PIRS 509b(revD) (1999).

[43] R. Brun, O. Couet, C. Vandoni, and P. Zanarini, PAW User Guide, CERN Computer Center, Geneva, Switzerland (1992).

[44] A. Kosunen and D. W. O. Rogers, ''Beam quality specification for photon beam dosimetry,'' Med. Phys. **20**, 1181–1188 (1993).

[45] P. Andreo and A. E. Nahum, ''Stopping-power ratio for a photon spectrum as a weighted sum of the values for monoenergetic photon beams,'' Phys. Med. Biol. **30**, 1055–1065 (1985).

[46] A. Booth and D. W. O. Rogers, Monte Carlo study of effects of phantom size, radial position, and depth on photon beam calibration, NRC Report PIRS-507, NRC Canada, Ottawa, K1A OR6, 1995.

[47] R. Mohan, C. Chui, and L. Lidofsky, ''Energy and angular distributions of photons from medical linear accelerators,'' Med. Phys. **12**, 592–597 (1985).

[48] D. W. O. Rogers, ''Low energy electron transport with EGS,'' Nucl. Instrum. Methods Phys. Res. A **227**, 535–548 (1984).

[49] A. F. Bielajew and D. W. O. Rogers, ''PRESTA: The parameter reduced electron-step transport algorithm for electron Monte Carlo transport,'' Nucl. Instrum. Methods Phys. Res. B **B18**, 165–181 (1987).

[50] IAEA, *The Use of Plane Parallel Ionization Chambers in High Energy Electron and Photon Beams: An International Code of Practice for Dosimetry*, Vol. 381 of *Technical Report Series* (IAEA, Vienna, 1997).

[51] P. R. Almond, P. J. Biggs, B. M. Coursey, W. F. Hanson, M. S. Huq, R. Nath, and D. W. O. Rogers, ''AAPM's TG-51 protocol for clinical reference dosimetry of high-energy photon and electron beams,'' Med. Phys. **26**, 1847–1870 (1999).